AGU PUBLICATIONS

Geophysical Research Letters

RESEARCH LETTER
10.1002/2016GL069079

Key Points:
- The EO-1 Hyperion spectrometer measured CH_4 from the Aliso Canyon release, achieving the first orbital detection of a CH_4 superemitter plume
- Multiple airborne observations by the AVIRIS-C imaging spectrometer corroborate the plume morphology and magnitude
- Empirical precision agrees with analytical instrument performance models and suggests potential for orbital superemitter surveys

Supporting Information:
- Supporting Information S1
- Dataset S1
- Dataset S2

Correspondence to:
D. R. Thompson,
david.r.thompson@jpl.nasa.gov

Citation:
Thompson, D. R., A. K. Thorpe, C. Frankenberg, R. O. Green, R. Duren, L. Guanter, A. Hollstein, E. Middleton, L. Ong, and S. Ungar (2016), Space-based remote imaging spectroscopy of the Aliso Canyon CH_4 superemitter, *Geophys. Res. Lett.*, *43*, 6571–6578, doi:10.1002/2016GL069079.

Received 25 APR 2016
Accepted 23 MAY 2016
Accepted article online 28 MAY 2016
Published online 20 JUN 2016

Space-based remote imaging spectroscopy of the Aliso Canyon CH_4 superemitter

D. R. Thompson[1], A. K. Thorpe[1], C. Frankenberg[1,2], R. O. Green[1], R. Duren[1], L. Guanter[3], A. Hollstein[3], E. Middleton[4], L. Ong[4], and S. Ungar[5]

[1]Jet Propulsion Laboratory, California Institute of Technology, Pasadena, California, USA, [2]Division of Geological and Planetary Sciences, California Institute of Technology, Pasadena, California, USA, [3]Helmholtz Centre Potsdam, GFZ German Research Centre for Geosciences, Potsdam, Germany, [4]NASA Goddard Space Flight Center, Greenbelt, Maryland, USA, [5]EO-1 Scientist Emeritus, NASA Goddard Space Flight Center, Greenbelt, Maryland, USA; Senior Research Scientist, Universities Space Research Association

Abstract The Aliso Canyon gas storage facility near Porter Ranch, California, produced a large accidental CH_4 release from October 2015 to February 2016. The Hyperion imaging spectrometer on board the EO-1 satellite successfully detected this event, achieving the first orbital attribution of CH_4 to a single anthropogenic superemitter. Hyperion measured shortwave infrared signatures of CH_4 near 2.3 μm at 0.01 μm spectral resolution and 30 m spatial resolution. It detected the plume on three overpasses, mapping its magnitude and morphology. These orbital observations were consistent with measurements by airborne instruments. We evaluate Hyperion instrument performance, draw implications for future orbital instruments, and extrapolate the potential for a global survey of CH_4 superemitters.

1. Introduction

On 23 October 2015, a well blowout was reported at the Aliso Canyon underground natural gas storage facility near Porter Ranch, California. A sustained release of CH_4 into the atmosphere continued until operators successfully capped the leak in February 2016 [*Conley et al.*, 2016]. The event was an extreme example of a CH_4*superemitter*, a class of anomalously large sources reported in studies of coal mines [*Krings et al.*, 2013] and oil and gas facilities [*Kort et al.*, 2014; *Rella et al.*, 2015; *Allen*, 2014; *Lyon et al.*, 2015; *Karion et al.*, 2015]. Superemitters are typically defined as a small number of sites or facilities with emissions large enough to dominate the CH_4 budgets of an area or economic sector [*Brandt et al.*, 2014]. Precise definitions vary by source sectors and regions. As one example, *Lyon et al.* [2015] report a heavy tail in the Barnett shale source population above 320 kg CH_4 h^{-1} for small gas processing plants and 750 kg CH_4 h^{-1} for large plants. Timely detection of superemitters would enable cost-effective greenhouse gas mitigation [*Zavala-Araiza et al.*, 2015], but monitoring infrastructure over large areas is challenging. The Aliso Canyon event occurred near a populated area, causing humanitarian disruption but offering a unique opportunity to demonstrate measurement strategies. The event was studied by a range of in situ sensors [*Conley et al.*, 2016] and NASA airborne remote sensing instruments including Airborne Visible/Infrared Imaging Spectrometer (AVIRIS-C) [*Green et al.*, 1998], and Hyperspectral Thermal Emission Spectrometer [*Hook et al.*, 2013]. Preliminary estimates of the Aliso Canyon gas leak suggest an unprecedented 20,000 kg CH_4 h^{-1} leak rate in January 2016 [*Conley et al.*, 2016].

This article reports detection of the Aliso Canyon release by the Hyperion imaging spectrometer on board the EO-1 spacecraft [*Folkman et al.*, 2001]. To our knowledge this was the first orbital attribution of a CH_4 superemitter plume from space. Hyperion measured reflected solar energy in visible through shortwave infrared wavelengths from 450–2400 nm at approximately 10 nm spectral sampling and 30 m spatial sampling. Hyperion was not designed for CH_4 detection, but its wavelength range captured a prominent 2300 nm CH_4 absorption band [*Thorpe et al.*, 2016a; *Thompson et al.*, 2015a]. After exhausting its fuel in 2011, the EO-1 spacecraft carrying Hyperion drifted earlier in the day from its original Sun-synchronous equatorial crossing time [*Middleton et al.*, 2013]. The winter season further reduced solar elevation and illumination to a level well below that of nominal instrument performance. Despite this handicap, Hyperion successfully detected the plume on multiple days. This suggests the potential for future orbital instruments with improved sensitivity such as Environmental Mapping and Analysis Program (EnMAP) [*Guanter et al.*, 2015],

or a spectrometer-equipped Landsat mission [*Mouroulis et al.*, 2016], to detect smaller and more numerous CH_4 superemitters from space. Such instruments, combined with wide-area survey capability, could improve constraints on point source contributions to the global atmospheric CH_4 growth rate and enable policymakers to better understand and address this unknown factor in greenhouse gas emissions. The following section describes the matched filter method used to map the Aliso Canyon CH_4 plume. We present results for spectral images from Hyperion and the AVIRIS-C airborne instrument [*Green et al.*, 1998]. We conclude with an evaluation of relative instrument performance, extrapolating sensitivities of future spectrometers such as EnMAP.

2. Method

Hyperion began collections over the Aliso Canyon site from December 2015, acquiring eight cloud-free observations (Table 1). The Hyperion calibration process translated Digital Numbers to radiance values in W cm^{-2} nm^{-1} sr^{-1}. We accounted for spectral smile by adjusting the wavelength calibration in pushbroom columns containing the source. Specifically, we fit the atmospheric water absorption feature near 1140 nm. We calculated atmospheric transmission using the ATmospheric REMoval (ATREM) atmospheric correction codebase [*Gao et al.*, 2009; *Thompson et al.*, 2015b] and resampled it to the Hyperion spectral response. Next, we shifted the Hyperion wavelength calibration to minimize the squared error fit to the continuum-removed radiance, treating the instrument full width at half maximum (FWHM) and scale of absorption as free parameters. For most scenes the resulting correction was under 5% of native sampling.

After refining the wavelength calibration, we measured CH_4 enhancements above the background by applying a matched filter independently to each cross-track location [*Thompson et al.*, 2015a]. We modeled the background radiance as a multivariate Gaussian with mean $\boldsymbol{\mu}$ and covariance $\boldsymbol{\Sigma}$, estimated from the data and regularized for stability by a small positive addition to diagonal elements [*Manolakis et al.*, 2007]. The matched filter tested the null hypothesis H_0 (that the spectrum $\mathbf{x}$ was generated by the background) against the alternative hypothesis H_1 (which included a perturbing signal $\mathbf{t}$ and scale factor α):

$$H_0 : \mathbf{x} \sim \mathcal{N}(\boldsymbol{\mu}, \boldsymbol{\Sigma}) \qquad H_1 : \mathbf{x} \sim \mathcal{N}(\boldsymbol{\mu} + \alpha\mathbf{t}, \boldsymbol{\Sigma}) \tag{1}$$

We followed the column-wise background estimation of *Thompson et al.* [2015a], ensuring most background pixels did not contain the plume. A slight contamination by the target signal would not impair detection performance [*Theiler and Foy*, 2006]. The matched filter $\hat{\alpha}(\mathbf{x})$ took the form:

$$\hat{\alpha}(\mathbf{x}) = (\mathbf{x} - \boldsymbol{\mu})^T \boldsymbol{\Sigma}^{-1} \mathbf{t} / \left(\mathbf{t}^T \boldsymbol{\Sigma}^{-1} \mathbf{t}\right). \tag{2}$$

This equation estimated the scaling factor α. As in *Thompson et al.* [2015a] we defined $\mathbf{t}$ to be the change in radiance caused a unit mixing ratio length of CH_4 absorption. This perturbation was a Beer-Lambert attenuation of the background $\boldsymbol{\mu}$, appropriate for optically thin CH_4 emissions enhancing the ambient CH_4. The partial derivative with respect to thickness ℓ of an absorbing CH_4 layer, taken at $\ell = 0$, was

$$\mathbf{t} = \partial\mathbf{x}/\partial\ell = -\boldsymbol{\mu} e^{-\boldsymbol{\kappa}\ell} = -\boldsymbol{\mu}\boldsymbol{\kappa}. \tag{3}$$

Here $\boldsymbol{\mu}$ represented the mean background radiance. We calculated the unit absorption coefficient of atmospheric CH_4, denoted κ, using the Reference Forward Model [*Dudhia*, 2014]. The detected quantity $\hat{\alpha}(\mathbf{x})$ was a mixing ratio length in units of pp·mm, the equivalent mixing ratio if the layer were 1 m thick. To translate this into a total column average, denoted XCH_4, for a scale height of about 8km [*Thorpe et al.*, 2014], we simply multiplied the mixing ratio length by 0.000125 m^{-1}. For example, 10,000 pp·mm translated to an XCH_4 enhancement of 1.25ppm.

The resulting enhancement images contained some sparse impulsive noise in isolated pixels. We addressed this by a spatial median filter [*Arce*, 2005] that replaced each image pixel with the median of its local 3×3 neighborhood. Finally, we calculated a physically interpretable plume strength, the Integrated Methane Enhancement, or IME, representing the total excess mass of CH_4. To compute this value, we manually marked and summed the contiguous pixels in each plume, scaling by the pixel surface area S according to

$$\mathrm{IME} = k \sum_{i=0}^{n} \hat{\alpha}(i) S(i). \tag{4}$$

Table 1. Hyperion Overpass Dates, Solar Elevations, Airmass Factors (AMF), and Integrated Methane Enhancement (IME) Values for Statistically Significant Detections[a]

Date	Solar Elevation	AMF	IME	Standard Error
29 Dec 2015	14.8°	5.0	710 kg	± 7.7 kg
01 Jan 2016	16.2°	4.6	1660	±9.0
12 Jan 2016	17.0°	4.4	-	-
26 Jan 2016	20.6°	4.0	-	-
03 Feb 2016	21.1°	3.8	460	±6.0
08 Feb 2016	19.5°	4.0	-	-
11 Feb 2016	21.8°	3.7	-	-
14 Feb 2016	24.1°	3.6	-	-

[a]Standard errors are calculated via root-sum-square via the estimated noise equivalent IME.

A constant, k, translated the integrated mixing ratio volume into CH_4 mass. We calculated detection significance p values using the empirical cumulative distribution function of the background [*Wasserman*, 2006], defined by a large rectangular region of >500 samples directly upwind of the plume and subtending the same pushbroom columns.

In addition to Hyperion, the plume was observed on multiple days by airborne instruments including NASA's "Classic" Airborne Visible Infrared Imaging Spectrometer (AVIRIS-C) [*Green et al.*, 1998]. AVIRIS-C measured the 380–2500 nm range with approximately 10 nm spectral sampling. It flew on board the ER-2 aircraft at 6600 m above ground level, providing 6.6 m spatial sampling. We performed a similar CH_4 detection with the AVIRIS-C data, with slight modifications to accommodate its unique characteristics. First, AVIRIS-C's whiskbroom design obviated the need for column-wise matched filtering. The extra samples provided by a unitary matched filter enabled a multimodal k-means background estimate as in *Funk et al.* [2001], with 10 clusters. This reduced interference by spectrally similar terrain features. Second, the fine spatial sampling of AVIRIS-C data made delineation of plume pixels more subjective so we automated that process to ensure consistency. We applied the normalized cuts routine of *Shi and Malik* [2000]; visual inspection confirmed segmentations' validity.

We evaluated the Hyperion and AVIRIS-C sensitivities using empirical noise estimates derived from scene data. We accumulated pairwise differences for neighboring locations of a flat region with uniform spectral albedo. This provided an accurate but model-free signal-to-noise ratio (SNR) estimate, which we applied to

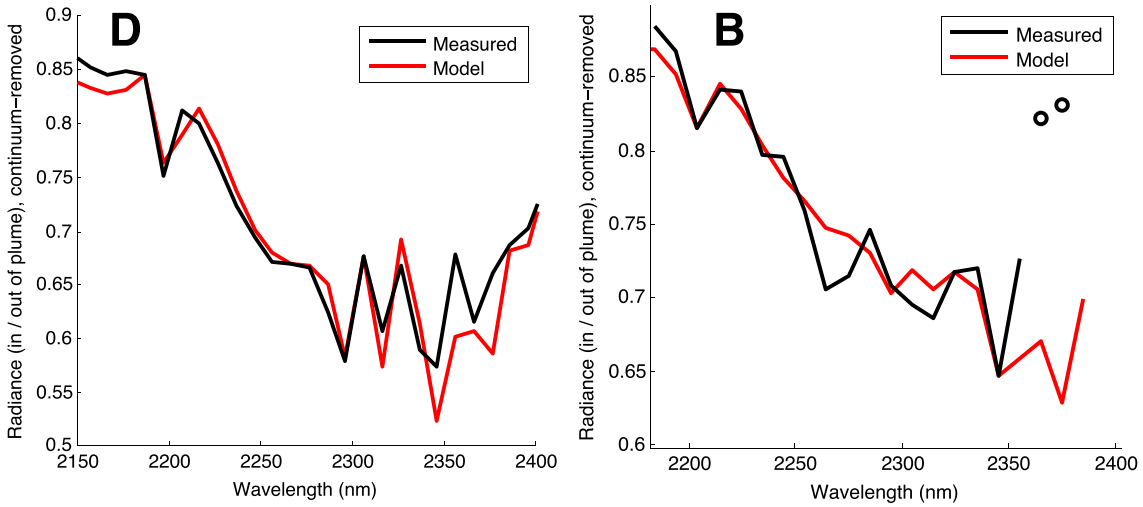

Figure 1. Measurements by AVIRIS-C on (left) 12 January 2016 and Hyperion on (right) 1 January 2016 both show CH_4 attenuation. The spectra show typical continuum-removed ratios of averaged regions inside and upwind of the plume. Measured ratios appear in black, and the best fitting CH_4 transmission model in red. Open circles show channels excluded from the fit due to systematic noise artifacts. The labels match plumes in Figures 2, 3, and 5 below.

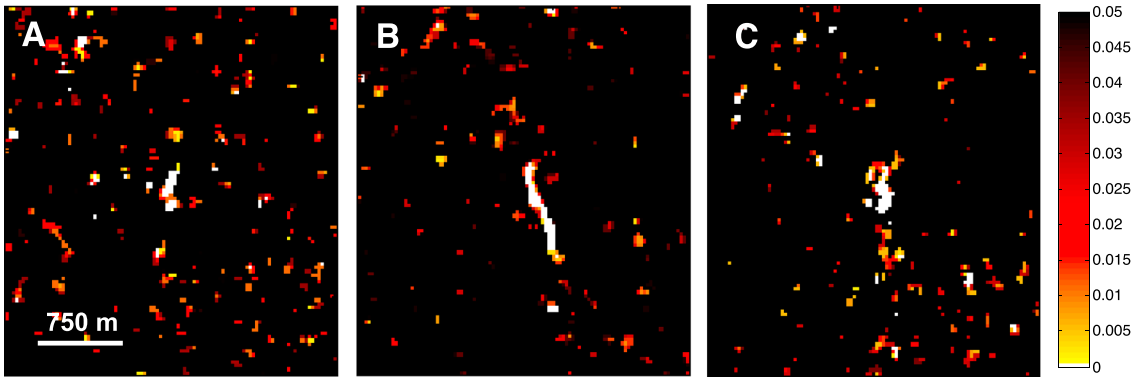

Figure 2. Statistically significant ($p \leq 0.05$) p values for each of the three Hyperion detection events, calculated independently for each pixel after spatial median filtering. (a) 29 December 2015. (b) 1 January 2016. (c) 3 February 2016. The labels match plumes in Figures 3 and 5.

a model radiance calculated from the LibRadTran radiative transfer routines [*Emde et al.*, 2015]. We propagated the SNR error estimate through the linearized detection algorithm to calculate a noise-equivalent mixing ratio length (NEMRL), and noise equivalent integrated methane enhancement (NEIME). This optimistic estimate ignored background clutter [*Theiler and Foy*, 2006] that might reduce sensitivity in complex environments. We compared these observed values for Hyperion and AVIRIS-C, as well as the Next Generation Airborne Visible Infrared Imaging Spectrometer (AVIRIS-NG) which has been used operationally for point source detection [*Thompson et al.*, 2015a; *Thorpe et al.*, 2016a]. Our AVIRIS-NG SNR estimates used reference surfaces from a recent campaign in the Four Corners area. Finally, we also evaluated characteristics of future orbital instruments.

3. Results

We calculate Hyperion and AVIRIS-C SNRs at 2300 nm to be 20 and 70, respectively. Hyperion is disadvantaged by intrinsic instrument characteristics and the solar elevation under 25°. However, three of eight cloud-free overpasses produce statistically significant detections. Figure 1 shows observed transmission spectra formed by ratioing radiances from inside and upwind of the plume. Red model lines show the best fitting CH_4 transmission, treating the CH_4 as a uniform layer and optimizing continuum offset, slope, and CH_4 absorption path length. Both instruments reveal a CH_4 enhancement, but the AVIRIS-C spectrum is the better match thanks to high sensitivity and more favorable midday illumination. The Hyperion profile diverges near 2400 nm due to low signal levels (SNR <5 in the longest wavelengths), but the location and morphology of the enhanced pixels is unambiguous. Figure 2 shows the detection events with p value scores for each

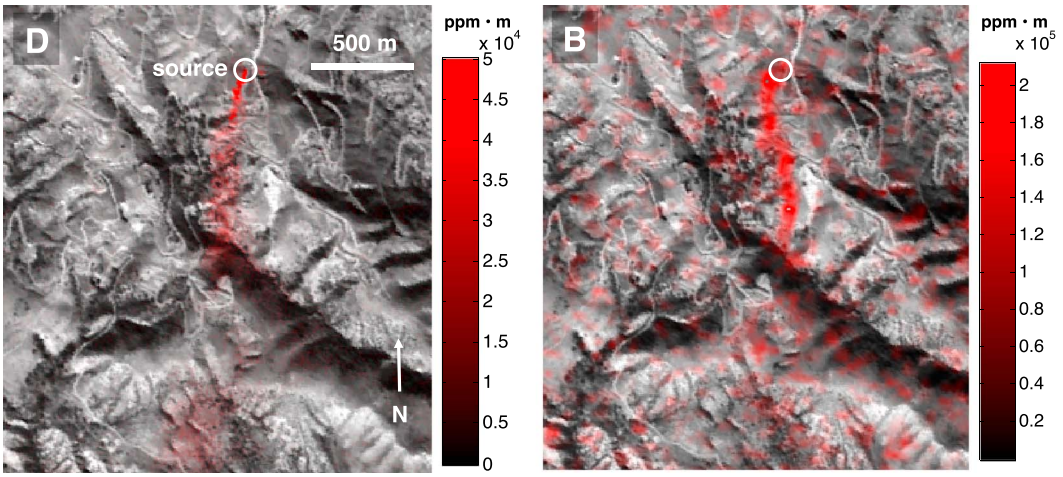

Figure 3. Comparison of detected plumes. D: AVIRIS-C flightline at 12 January 2016, 20:25 UTC. B: Hyperion on 1 January 2016, 16:39 UTC. The labels match plumes in Figures 2 and 5.

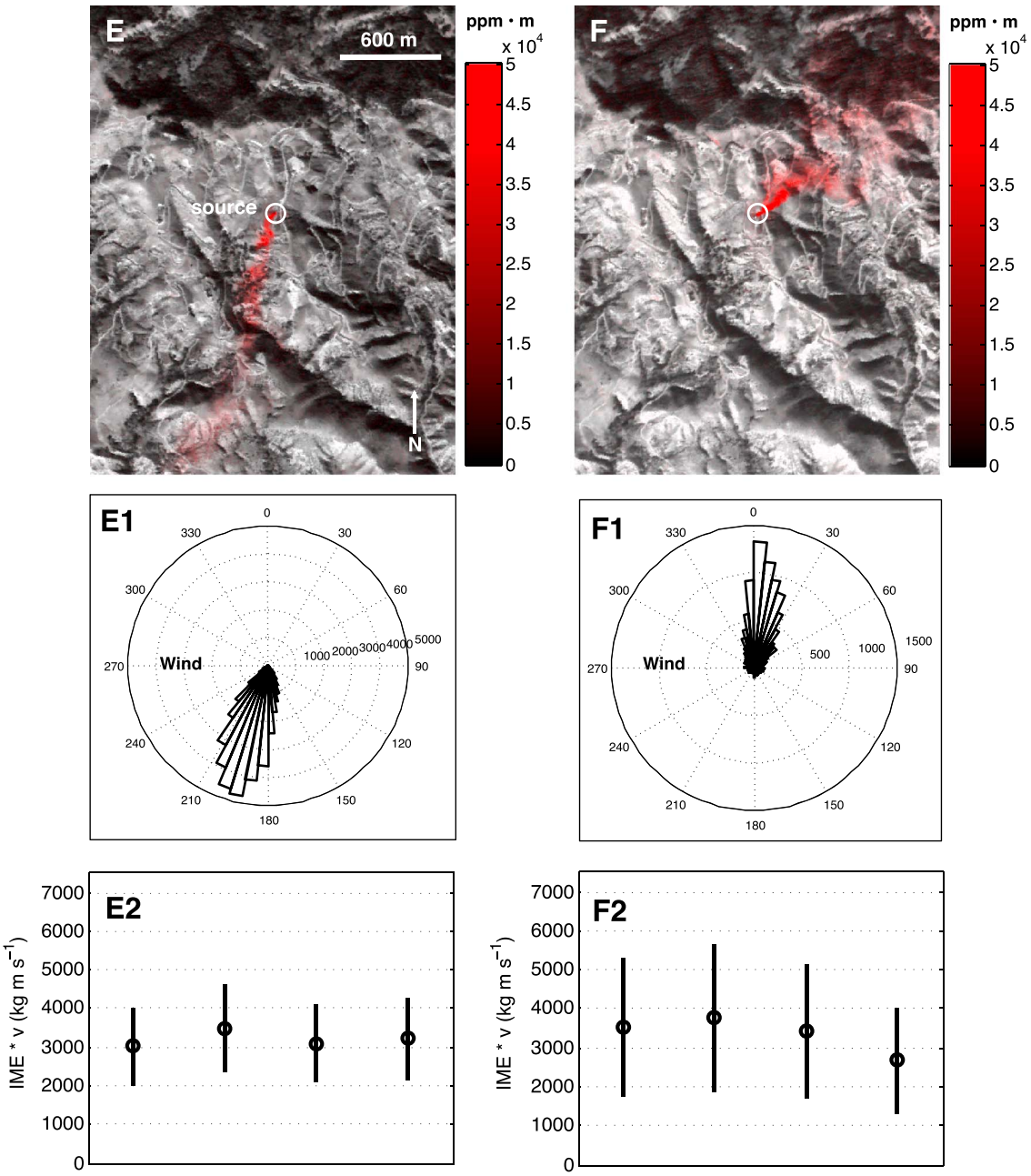

Figure 4. Comparison of detected plumes from AVIRIS-C under different wind conditions. Labels correspond to specific days in Figure 5. E: Retrieved CH_4 mixing ratio length on 12 January 2016, 20:41 UTC. E1: The frequency of wind direction within 2 h of the aircraft overpass, sampled at 0.25 Hz by a nearby sonic anemometer. E2: Corrected IME · *v*, formed by integrating the plume CH_4 mass inside a bounded distance of 500 m and scaling by the wind speed. 1σ error bars indicate wind variability. F: CH_4 on 14 January 2016, 21:36 UTC. F1: Wind directions on 14 January F2: IME · *v* as in E2, with 1σ error bars.

median-filtered pixel. Bright clusters in the centers of significant to *p* values of <0.005. We use letters A–F to reference plumes in Figures 2–5.

The two sensors reveal similar plume morphologies. Figure 3 compares an AVIRIS-C detection on 12 January and the strongest Hyperion detection on 1 January, georectified and overlayed in red on the 2300 nm AVIRIS-C channel. In both cases winds from the north cause a mostly laminar plume extending south into the valley. On some other days, occasional winds from the south result in turbulent CH_4 accumulations along the hillside. These two conditions show distinct IME profiles. Figure 4 illustrates this with plumes on 12 and 14 January. Rose histograms show wind directions within 2 h of the AVIRIS-C overpass as measured at 4 Hz by a sonic

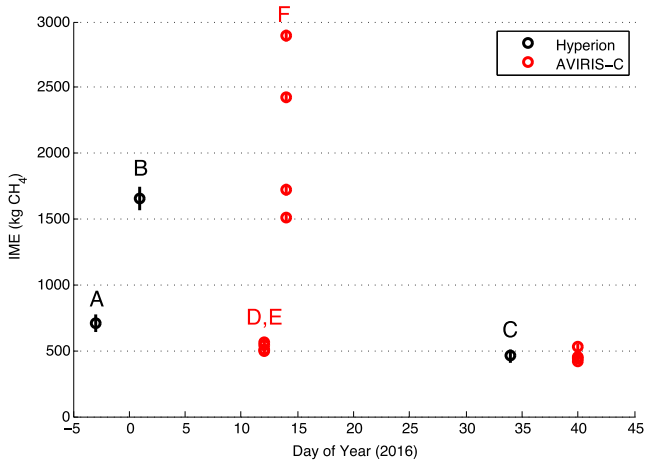

Figure 5. Comparison of IME values from Hyperion and AVIRIS-C. For the AVIRIS-C overpass days, multiple points represent the first four flightlines over the source, spanning multiple viewing azimuth angles. Letters indicate data associated with panels in Figures 2–4. Error bars indicate 2σ (95%) noise intervals on the integrated IME measurement. Most error bars lie within the marker widths; they exclude wind variability and consequently understate observed changes in plume intensity.

anemometer near the site. Measured wind speeds on 12 January average 6.1 ± 2.0 m s^{-1} (1σ). On 14 January they are significantly lower, but with higher relative variability, averaging 2.5 ± 1.3 m s^{-1} (1σ). Panels E2 and F2 correct the IME of each overflight by integrating the plume CH_4 mass enhancement within 500 m from the source and scaling by the ambient wind speed. Error bars indicate the wind standard deviation. This shows agreement between the 2 days despite winds that differ by 180° in direction and over 100% in magnitude. The 12 January overflight provides near temporal coincidence of measurements between AVIRIS-C and the in situ sampling of *Conley et al.* [2016] who estimate a flux of 20,700 ± 3100 kg h^{-1} on that day.

Figure 5 summarizes AVIRIS-C and Hyperion IME values with multiple AVIRIS-C overpasses appearing as distinct points. Error bars indicate measurement noise calculated from the distribution of background detection signals outside the plume. Standard error of the total IME measurement is very small due to the root-sum-square noise reduction from aggregating many plume pixels, making the spread of values from different overflights a better indicator of variability. Most measurements indicate consistent IME values near 500 kg CH_4. On 14 January values increase by a factor of 2–5, consistent with the uniquely low wind speeds and high wind variability described above.

Table 2 shows the relative sensitivity of Hyperion, AVIRIS-C, and AVIRIS-NG from empirical noise estimates. We also include NEMRL and NEIME values for projected sensors: a spectrometer-equipped Landsat continuity

Table 2. Sensitivity for Current and Proposed Instruments Under Typical Observing Conditions[a]

Scenario	Albedo	Solar Elevation	SNR	FWHM	GSD	NEMRL	NEIME	Reference
Hyperion	–	16.2°	20[b]	10 nm	30 m	1825 ppm·m	1.17 kg	This work
AVIRIS-C	–	33°	70[b]	10	6.6	521	0.016	This work
AVIRIS-NG	–	64°	200[b]	5	4	124	0.001	This work
EnMAP	0.3	60°	180[c]	10	30	202	0.13	[*Guanter et al.*, 2015]
Landsat Swath Dyson	0.25	66.5°	200[c]	6.8	30	146	0.09	[*Mouroulis et al.*, 2016]
AMPS airborne	0.2	41.8°	175[c]	1	1	54	0.0000383	[*Thorpe et al.*, 2016b]

[a]SNR estimates for existing instruments use actual scene data from desert terrain with minimal vegetation. Future instruments presented in the last three rows simulate SNR over a uniform surface of known albedo. SNR: signal-to-noise ratio. FWHM: Spectral resolution, full width at half maximum. GSD: Ground Sampling Distance. NEMRL: noise-equivalent mixing ratio length (per spectrum). NEIME: noise-equivalent integrated methane enhancement (per spectrum). Overall, these scenarios use different illumination and albedo conditions so they are intended as reference points rather than performance benchmarks.
[b]Empirical noise estimate.
[c]Projected noise estimate.

mission [*Mouroulis et al.*, 2016], the Airborne Methane Plume Spectrometer (AMPS) [*Thorpe et al.*, 2016b], and EnMAP [*Guanter et al.*, 2015]. Note that SNR estimates are not directly comparable across different observing conditions, so the table entries are intended as reference examples rather than performance benchmarks. The sensitivity estimates from error propagation are consistent with prior airborne studies. For example, *Thompson et al.* [2015a] calculated an empirical NEMRL of 146 pp·mm directly from AVIRIS-NG observations of many plumes. Our pure analytical estimate matched that value within 20%; any difference could be explained completely by variability in substrate and illumination.

4. Discussion

Prior and ongoing studies have demonstrated the ability of airborne infrared imaging spectrometers for surveying and quantifying CH_4 point sources [*Thompson et al.*, 2015a]. The Aliso Canyon event now demonstrates that similar surveys are possible from orbit. During this event, the Hyperion instrument was severely handicapped with solar elevations less than 25° resulting in low incident illumination and topographic cast shadows. Consequently, it is not surprising that some overpasses did not result in significant detections. Variable wind conditions in the mountainous Aliso Canyon terrain posed another challenge; they could have dispersed the plume, carried it over shaded or low-albedo regions, or fragmented the contiguity of single pixel enhancements. However, a correspondence of spectral, spatial, and multi-instrument evidence suggests that Hyperion successfully detected the Aliso Canyon event on 3 days over a period of a month. Plume morphologies and magnitude estimates were consistent across the airborne and space-based instruments.

In practice, the Ground Sampling Distance (GSD), which is 30 m or more for anticipated orbital missions, may be an important factor controlling sensitivity vis-a-vis airborne campaigns. Larger GSDs require a sizable plume to fully subtend pixels and accumulate nominal mixing ratio lengths. Airborne studies of coal mines and gas facilities have observed many plumes of relevant spatial extent. The launch of EnMAP [*Guanter et al.*, 2015] will enable targeted observations of suspected superemitters under more favorable observing conditions to initiate a global catalog. A global mapping mission such as a Landsat swath imaging spectrometer [*Mouroulis et al.*, 2016] would be a natural next step beyond Hyperion. It would cover the globe's terrestrial surfaces in 185 km swaths at 30 m resolution to enable a comprehensive survey capable of identifying the largest emitters and tracking their changes over time. Dedicated CH_4 mapping with higher spectral resolution [*Thorpe et al.*, 2016a] would also allow more robust quantitative retrievals and much enhanced Table 2. This would be a major step forward in quantifying CH_4 superemitters' contribution to anthropogenic radiative forcing.

Acknowledgments

We Acknowledge support from the NASA Earth Science Division and the program for Rapid Response and Novel Research in Earth Sciences. AVIRIS-C data are available from http://aviris.jpl.nasa.gov. AVIRIS-NG data are available from http://avirisng.jpl.nasa.gov. Hyperion data are available from http://earthexplorer.usgs.gov. We thank Stuart Frye of Goddard Space Flight Center who played a central role in acquiring the Hyperion observations. We acknowledge and thank the AVIRIS-C flight team, including Sarah Lundeen, Ian McCubbin, and Charles Sarture. We also thank scientists at JPL and elsewhere whose counsel was invaluable throughout the system design process: Andrew Aubrey, Lance Christensen, Dar A. Roberts, and Brian Bue. AVIRIS-C is sponsored by the NASA Earth Science Division. A portion of the research described in this paper was performed by the Jet Propulsion Laboratory, California Institute of Technology, under a contract with the National Aeronautics and Space Administration. We acknowledge and thank Stephen Conley, University of California Davis.

References

Allen, D. T. (2014), Methane emissions from natural gas production and use: Reconciling bottom-up and top-down measurements, *Curr. Opin. Chem. Eng.*, *5*, 78–83.

Arce, G. R. (2005), *Nonlinear Signal Processing: A Statistical Approach*, John Wiley.

Brandt, A., et al. (2014), Methane leaks from north american natural gas systems, *Science*, *343*(6172), 733–735.

Conley, S., G. Franco, I. Faloona, D. R. Blake, J. Peischl, and T. B. Ryerson (2016), Methane emissions from the 2015 Aliso Canyon blowout in Los Angeles, CA, *Science*, *351*(6279), 1317–1320, doi:10.1126/science.aaf2348.

Dudhia, A. (2014), *Oxford University Reference Forward Model (RFM)*. [Available at http://www.atm.ox.ac.uk/RFM/.]

Emde, C., et al. (2015), The libradtran software package for radiative transfer calculations (version 2.0), *Geosci. Model Dev. Discuss.*, *8*, 10,237–10,303, doi:10.5194/gmdd-8-10237-2015.

Folkman, M. A., J. Pearlman, L. B. Liao, and P. J. Jarecke (2001), EO-1/Hyperion hyperspectral imager design, development, characterization, and calibration, *Proc. SPIE*, *4151*, 40–51.

Funk, C. C., J. Theiler, D. A. Roberts, and C. C. Borel (2001), Clustering to improve matched filter detection of weak gas plumes in hyperspectral thermal imagery, *IEEE Trans. Geosci. Remote Sens.*, *39*(7), 1410–1420.

Gao, B.-C., M. J. Montes, C. O. Davis, and A. F. Goetz (2009), Atmospheric correction algorithms for hyperspectral remote sensing data of land and ocean, *Remote Sens. Environ.*, *113*, S17–S24.

Green, R. O., et al. (1998), Imaging spectroscopy and the Airborne Visible/Infrared Imaging Spectrometer (AVIRIS), *Remote Sens. Environ.*, *65*(3), 227–248.

Guanter, L., et al. (2015), The EnMAP spaceborne imaging spectroscopy mission for Earth observation, *Remote Sens.*, *7*(7), 8830–8857.

Hook, S. J., W. R. Johnson, and M. J. Abrams (2013), NASA's Hyperspectral Thermal Emission Spectrometer (HyTES), in *Thermal Infrared Remote Sensing*, edited by C. Kuenza and S. Dech, pp. 532, Springer, doi:10.1007/978-94-007-6639-6.

Karion, A., et al. (2015), Aircraft-based estimate of total methane emissions from the Barnett shale region, *Environ. Sci. Technol.*, *49*(13), 8124–8131, doi:10.1021/acs.est.5b00217.

Kort, E. A., C. Frankenberg, K. R. Costigan, R. Lindenmaier, M. K. Dubey, and D. Wunch (2014), Four Corners: The largest US methane anomaly viewed from space, *Geophys. Res. Lett.*, *41*, 6898–6903, doi:10.1002/2014GL061503.

Krings, T., K. Gerilowski, M. Buchwitz, J. Hartmann, T. Sachs, J. Erzinger, J. P. Burrows, and H. Bovensmann (2013), Quantification of methane emission rates from coal mine ventilation shafts using airborne remote sensing data, *Atmos. Meas. Tech.*, *6*(1), 151–166, doi:10.5194/amt-6-151-2013.

Lyon, D. R., et al. (2015), Constructing a spatially resolved methane emission inventory for the Barnett shale region, *Environ. Sci. Technol.*, *49*(13), 8147–8157.

Manolakis, D., R. Lockwood, T. Cooley, and J. Jacobson (2007), Robust matched filters for target detection in hyperspectral imaging data, in *IEEE International Conference on Acoustics, Speech and Signal Processing (ICASSP '07)*, vol. 1, pp. I-529–I-532, IEEE, Honolulu, Hawaii.

Middleton, E. M., S. G. Ungar, D. J. Mandl, L. Ong, S. W. Frye, P. E. Campbell, D. R. Landis, J. P. Young, and N. H. Pollack (2013), The earth observing one (EO-1) satellite mission: Over a decade in space, *IEEE J. Sel. Top. Appl. Earth Observations Remote Sens.*, *6*(2), 243–256.

Mouroulis, P., R. O. Green, B. Van Gorp, L. B. Moore, D. W. Wilson, and H. A. Bender (2016), Landsat swath imaging spectrometer design, *Opt. Eng.*, *55*(1), 15104, doi:10.1117/1.OE.55.1.015104.

Rella, C. W., T. R. Tsai, C. G. Botkin, E. R. Crosson, and D. Steele (2015), Measuring emissions from oil and natural gas well pads using the mobile flux plane technique, *Environ. Sci. Technol.*, *49*(7), 4742–4748.

Shi, J., and J. Malik (2000), Normalized cuts and image segmentation, *IEEE Trans. Pattern Anal. Machine Intelligence*, *22*(8), 888–905.

Theiler, J., and B. R. Foy (2006), Effect of signal contamination in matched-filter detection of the signal on a cluttered background, *IEEE Geosci. Remote Sens. Lett.*, *3*(1), 98–102.

Thompson, D. R., et al. (2015a), Real-time remote detection and measurement for airborne imaging spectroscopy: A case study with methane, *Atmos. Meas. Tech.*, *8*(10), 4383–4397, doi:10.5194/amt-8-4383-2015.

Thompson, D. R., B.-C. Gao, R. O. Green, D. A. Roberts, P. E. Dennison, and S. R. Lundeen (2015b), Atmospheric correction for global mapping spectroscopy: ATREM advances for the HyspIRI preparatory campaign, *Remote Sens. Environ.*, *167*, 64–77.

Thorpe, A., et al. (2016a), Mapping methane concentrations from a controlled release experiment using the next generation Airborne Visible/Infrared Imaging Spectrometer (AVIRIS-NG), *Remote Sens. Environ.*, *179*, 104–115, doi:10.1016/j.rse.2016.03.032.

Thorpe, A. K., C. Frankenberg, and D. A. Roberts (2014), Retrieval techniques for airborne imaging of methane concentrations using high spatial and moderate spectral resolution: Application to AVIRIS, *Atmos. Meas. Tech.*, *7*(2), 491–506, doi:10.5194/amt-7-491-2014.

Thorpe, A. K., C. Frankenberg, R. O. Green, D. R. Thompson, A. D. Aubrey, P. Mouroulis, M. L. Eastwood, and G. Matheou (2016b), The Airborne Methane Plume Spectrometer (AMPS): Quantitative imaging of methane plumes in real time, in *Proceedings of IEEE Conference, volume 6.0301*, Big Sky, Mont., 4–11 March. [Available at www.aeroconf.org.]

Wasserman, L. (2006), *All of Nonparametric Statistics (Springer Texts in Statistics)*, Springer, New York, Inc., Secaucus, N. J.

Zavala-Araiza, D., et al. (2015), Reconciling divergent estimates of oil and gas methane emissions, *Proc. Natl. Acad. Sci.*, *112*(51), 15,597–15,602, doi:10.1073/pnas.1522126112.